

## A Numerical Study of the Flow past an Normally Oscillating Circular Cylinder

**Danilo Gonçalves Carneiro**

University of Brasilia, Brasilia, DF, 70910-900, Brazil  
danilocarneiro@gmail.com

**Roberto Francisco Bobenrieth Miserda**

University of Brasilia, Brasilia, DF, 70910-900, Brazil  
rfbm@unb.br

**Abstract.** *The objective of this work is the numerical simulation of the two-dimensional laminar flow over a circular cylinder with a forced normal oscillation in order to asset the effect of different combinations of the cylinder's maximum linear velocity and angular frequency on the dynamic response of the system in terms of the resultant aerodynamic coefficients. The system of equations is written using a non-inertial frame of reference that is fixed to the oscillating circular cylinder. The effect of this motion is accounted by the introduction of pseudo-force and pseudo-work terms in the right-hand side of the compressible Navier-Stokes equations. These equations are numerically solved using a finite volume discretization, and the fluxes of mass, momentum and total energy are evaluated using the anti-symmetric form of Ducros' fourth-order numerical method. The time marching is achieved using the third-order Runge-Kutta method proposed by Shu. The linear amplitude of vertical motion is defined as sinusoidal in time with an angular frequency tied to the simulated vortex-emission frequency of the static circular cylinder. The system response to different combinations of velocities and frequencies showed different kinds of vortex systems topologies and different behaviors of the unsteady aerodynamic coefficients. These responses were periodic and symmetric, periodic and anti-symmetric, pre-chaotic and even chaotic.*

**Keywords:** *Numerical Simulation, Circular Cylinder, Normal Oscillation, Laminar Flow, Non-Inertial Frame*

### 1. Introduction

The main purpose of the present work is the numerical simulation of the laminar flow over a circular cylinder submitted to a forced normal oscillation. Flows over circular cylinders are present in several areas of engineering, as structural design, especially high towers and transmission cables of electrical energy, that are usually submitted to strong winds, offshore structures, thermo-fluids, aerospace sciences, where the landing gear, for example, is commonly submitted to strong winds and aerodynamic forces, among others. These kinds of flows, as they generate vortex-streets, induce unsteady aerodynamic forces over the structure capable of developing oscillation motions that can even destruct the structure by fracture. Being so, a good understanding of the vortex- street topology and the behavior of the unsteady aerodynamics coefficients, is essential.

Previous work, Jared *et al* (1997), showed the behavior of the flow over a static circular cylinder in a considerable range of Reynolds number using numerical simulations that had laminar model and also turbulent models. Blackburn and Henderson (1999), showed in their work an analysis of the laminar flow over an oscillating circular cylinder in cross flow, fixing the Reynolds number to 500 and varying the ratio between the oscillation frequency of the cylinder and the natural vortex-emission frequency. The main objective of their work was to determine how this variation changes the aerodynamic forces utilizing an incompressible formulation and analyzing only the near-wake region.

In order to simulate the normal oscillation of the circular cylinder using a compressible formulation and analyzing the effect of different combinations of the cylinder's maximum linear velocity and angular frequency on the dynamic response of the system in terms of the resultant aerodynamic coefficients, the compressible Navier-Stokes equations are modified in this work using the concept of pseudo-forces and pseudo-work in order to represent the oscillation of the cylinder from a non-inertial frame of reference. They are solved using Ducros' fourth-order skew-symmetric scheme for calculating the fluxes in a finite-volume discretization in conjunction with a third-order Runge-Kutta time-marching method, as proposed by Bobenrieth Miserda and Mendonça (2005).

### 2. Mathematical Model

The system of equation utilized in the present work is written using a non inertial frame of reference fixed to the oscillating circular cylinder. The effect of this motion is accounted by a pseudo-force term in the right-hand side of the momentum equation that acts as a body force, Batchelor (1983). In similar manner, the work done by this pseudo-force is accounted by a pseudo-work term in the right-hand side of the energy equation. With these considerations, the nondimensional form of the Navier-Stokes equations can be written as:

$$\frac{\partial \rho}{\partial t} + \frac{\partial}{\partial x_i}(\rho u_i) = 0 \quad (1)$$

$$\frac{\partial}{\partial t}(\rho u_i) + \frac{\partial}{\partial x_j}(\rho u_i u_j) = -\frac{\partial p}{\partial x_i} + \frac{\partial \tau_{ij}}{\partial x_j} + f_i \quad (2)$$

$$\frac{\partial}{\partial t}(\rho e_T) + \frac{\partial}{\partial x_i}(\rho e_T u_i) = -\frac{\partial}{\partial x_i}(p u_i) + \frac{\partial}{\partial x_i}(\tau_{ij} u_j) - \frac{\partial q_{x_i}}{\partial x_i} + f_i u_i \quad (3)$$

In the equations above all the variables are in a nondimensional form:  $\rho$  is the density,  $t$  is the temporal coordinate,  $u_i$  is the  $i$ -direction component of the velocity vector,  $x_i$  is the  $i$ -direction spatial coordinate,  $p$  is the pressure,  $\tau_{ij}$  is the stress tensor,  $f_i$  is the pseudo-force due to the oscillating motion,  $e_T$  is the total energy per unit of mass and  $q_{x_i}$  is the heat-flow density in the  $i$ -direction

The nondimensional form of the flow variables and properties are obtained using the following relations:

$$\begin{aligned} x_i &= \frac{x_i^*}{d^*}, & u_i &= \frac{u_i^*}{U_\infty^*}, & t &= \frac{t^*}{d^*/U_\infty^*}, & p &= \frac{p^*}{\rho_\infty^* (U_\infty^*)^2}, & \rho &= \frac{\rho^*}{\rho_\infty^*}, & e_T &= \frac{e_T^*}{(U_\infty^*)^2}, \\ \mu &= \frac{\mu^*}{\mu_\infty^*}, & e &= \frac{e^*}{(U_\infty^*)^2}, & e_k &= \frac{e_k^*}{(U_\infty^*)^2}, & c_v &= \left[ \frac{T_\infty^*}{(U_\infty^*)^2} \right] c_v^*, & T &= \frac{T^*}{T_\infty^*}, \end{aligned} \quad (4)$$

where the asterisk denotes dimensional quantities and  $x_i^*$  is the  $i$ -direction spatial coordinate,  $d^*$  is the cylinder's diameter,  $U_\infty^*$  is the undisturbed velocity magnitude,  $t^*$  is the temporal coordinate,  $p^*$  is the pressure,  $\rho^*$  is the density,  $\rho_\infty^*$  is the density of the undisturbed flow,  $e_T^*$  is the total energy per unit of mass,  $\mu$  is the nondimensional dynamic viscosity  $\mu^*$  is the dynamic viscosity  $\mu_\infty^*$  is the dynamic viscosity of the undisturbed flow,  $e$  is the nondimensional internal energy per unit mass,  $e^*$  is the internal energy per unit mass,  $e_k$  is the nondimensional kinetic energy per unit mass,  $e_k^*$  is the kinetic energy per unit mass,  $c_v$  is the nondimensional specific heat at constant volume  $c_v^*$  is the specific heat at constant volume,  $T$  is the nondimensional temperature  $T^*$  is the temperature and  $T_\infty^*$  is the temperature of the undisturbed flow. The nondimensional viscous stress tensor is given by

$$\tau_{ij} = \frac{1}{\text{Re}} (\mu S_{ij}) = \frac{1}{\text{Re}} \left\{ \mu \left[ \left( \frac{\partial u_i}{\partial x_j} + \frac{\partial u_j}{\partial x_i} \right) - \frac{2}{3} \delta_{ij} \frac{\partial u_k}{\partial x_k} \right] \right\} \quad (5)$$

where  $S_{ij}$  is the nondimensional rate-of-strain tensor,  $\delta_{ij}$  is the Kronecker delta and the Reynolds number is defined as

$$\text{Re} = \frac{\rho_\infty^* U_\infty^* d^*}{\mu_\infty^*} \quad (6)$$

The total energy is given by the sum of the internal and kinetic specific energy as

$$e_T = e + e_k = c_v T + \frac{u_i u_i}{2} \quad (7)$$

and the nondimensional heat flux density, where  $\gamma$  is the specific heat ratio, is given by

$$q_{x_i} = -\frac{\mu}{(\gamma - 1) M^2 \text{Re Pr}} \left( \frac{\partial T}{\partial x_i} \right) \quad (8)$$

In Eq. (8),  $M$  is the Mach number and  $Pr$  is the Prandtl number, being defined as

$$M = \frac{U_{\infty}^*}{\sqrt{\gamma R^* T_{\infty}^*}}, \quad Pr = \frac{c_p^*}{k_{\infty}^*} \mu_{\infty}^* \quad (9)$$

where  $R$  is the specific gas constant,  $c_p^*$  is the specific heat at constant pressure and  $k_{\infty}^*$  is the thermal conductivity of the undisturbed flow.

In the present work, the Prandtl number is assumed to be a constant with the value  $Pr = 0.72$ . Being so, for a thermally and calorically perfect gas, the nondimensional equation of state assume the following form

$$p = (\gamma - 1) \rho e \quad (10)$$

and

$$T = \frac{\gamma M^2 p}{\rho} \quad (11)$$

The nondimensional molecular viscosity is obtained using Sutherland's formula

$$\mu = C_1 \frac{T^{3/2}}{T + C_2}, \quad C_1 = \left[ \frac{(T_{\infty}^*)^{1/2}}{\mu_{\infty}^*} \right] C_1^*, \quad C_2 = \frac{C_2^*}{T_{\infty}^*}. \quad (12)$$

where  $C_1$  is the nondimensional first gas constant in Sutherland's formula,  $C_1^*$  is the first gas constant in Sutherland's formula,  $C_2$  is the nondimensional second gas constant in Sutherland's formula and  $C_2^*$  is the second gas constant in Sutherland's formula.

As the primary objective of this work is to analyze the effect of the oscillating motion over the resulting aerodynamic forces, the pseudo-force,  $f_i$  that appears in Equations (2) and (3), accounts for this motion when the Navier-Stokes equations are written for a non-inertial frame or reference. The imposed motion has a sinusoidal linear amplitude in time and the components of the pseudo-force,  $f_i$  are given by

$$f_i = \frac{1}{2} \rho A_i \omega_i^2 \sin(\omega_i t) \quad (13)$$

where the nondimensional maximum amplitude,  $A_i$ , and angular frequency,  $\omega_i$ , are defined as

$$A_i = \frac{A_i^*}{d^*}, \quad \omega_i = \frac{\omega_i^*}{U_{\infty}^*/d^*}. \quad (14)$$

with  $A^*$  and  $\omega^*$  being the maximum amplitude of motion and angular frequency of the sinusoidal motion respectively.

The boundary conditions at the wall of the circular cylinder are a no-slip condition for the velocity field, an adiabatic wall for the temperature field and a null gradient in the normal direction at the wall for the pressure field.

### 3. Numerical Method

Since the geometry of interest is a circular cylinder and the flow is laminar, the two-dimensional form of the Navier-Stokes equations is used. In order to numerically solve these equations using a finite volume approach, Equations (1), (2) and (3) are written in the following vector form, Anderson *et al.* (1983):

$$\frac{\partial \mathbf{U}}{\partial t} + \frac{\partial \mathbf{E}}{\partial x} + \frac{\partial \mathbf{F}}{\partial y} = \mathbf{R} \quad (15)$$

where  $\mathbf{U}$  is the nondimensional conservative-variables vector,  $\mathbf{E}$  and  $\mathbf{F}$  are nondimensional flux vectors and  $\mathbf{R}$  is the nondimensional vector associated with the oscillating motion. The first three vectors are given by

$$\mathbf{U} = \begin{bmatrix} \rho \\ \rho u \\ \rho v \\ \rho e_T \end{bmatrix}, \quad \mathbf{E} = \begin{bmatrix} \rho u \\ \rho u^2 + p - \tau_{xx} \\ \rho uv - \tau_{xy} \\ (\rho e_T + p)u - u\tau_{xx} - v\tau_{xy} + q_x \end{bmatrix}, \quad \mathbf{F} = \begin{bmatrix} \rho v \\ \rho vu - \tau_{xy} \\ \rho v^2 + p - \tau_{yy} \\ (\rho e_T + p)v - u\tau_{xy} - v\tau_{yy} + q_y \end{bmatrix}. \quad (16)$$

where  $u$  is the nondimensional  $x$ -direction component of the velocity vector and  $v$  is the nondimensional  $y$ -direction component of the velocity vector.

The oscillating motion of the cylinder in this work is imposed in the  $y$ -direction, and consequently, the  $\mathbf{R}$  vector is defined as:

$$\mathbf{R} = \begin{bmatrix} 0 \\ 0 \\ \frac{1}{2} \rho A_y \omega_y^2 \sin(\omega_y t) \\ \frac{1}{2} \rho A_y \omega_y^2 \sin(\omega_y t) v \end{bmatrix}. \quad (17)$$

Defining the flux tensor  $\Pi$  as

$$\Pi = \mathbf{E} \otimes \mathbf{i} + \mathbf{F} \otimes \mathbf{j} \quad (18)$$

Equation (15) can now be written as

$$\frac{\partial \mathbf{U}}{\partial t} + \nabla \cdot \Pi = \mathbf{R} \quad (19)$$

Integrating Eq. (19) over the control volume  $V$ , and applying the divergence theorem to the first term of right-hand side results

$$\frac{\partial}{\partial t} \int_V \mathbf{U} dV = - \int_V (\nabla \cdot \Pi) dV + \int_V \mathbf{R} dV = - \int_S (\Pi \cdot \mathbf{n}) dS + \int_V \mathbf{R} dV \quad (20)$$

where  $S$  is the surface of control and  $\mathbf{n}$  is the normal unit vector. Defining the volumetric mean of vectors  $\mathbf{U}$  and  $\mathbf{R}$  in the control volume  $V$  as

$$\bar{\mathbf{U}} \equiv \frac{1}{V} \int_V \mathbf{U} dV, \quad \bar{\mathbf{R}} \equiv \frac{1}{V} \int_V \mathbf{R} dV, \quad (21)$$

Equation (20) can be written as

$$\frac{\partial \bar{\mathbf{U}}}{\partial t} = - \frac{1}{V} \int_S (\Pi \cdot \mathbf{n}) dS + \bar{\mathbf{R}} \quad (22)$$

For the volume  $(i, j)$ , the first-order approximation of the temporal derivative is given by

$$\left( \frac{\partial \bar{\mathbf{U}}}{\partial t} \right)_{i,j} = \frac{\Delta \bar{\mathbf{U}}_{i,j}}{\Delta t} + O(\Delta t) \quad (23)$$

where  $\Delta \bar{\mathbf{U}}_{i,j}$  is the variation of the nondimensional conservative-variables vector and  $\Delta t$  is the nondimensional time step. The temporal approximation of Eq. (22) for a quadrilateral and two-dimensional control volume is

$$\Delta \bar{\mathbf{U}}_{i,j} = -\frac{\Delta t}{V_{i,j}} \left[ \int_{S_{i+1/2}} (\boldsymbol{\Pi} \cdot \mathbf{n}) dS + \int_{S_{i-1/2}} (\boldsymbol{\Pi} \cdot \mathbf{n}) dS + \int_{S_{j+1/2}} (\boldsymbol{\Pi} \cdot \mathbf{n}) dS + \int_{S_{j-1/2}} (\boldsymbol{\Pi} \cdot \mathbf{n}) dS \right] + \Delta t \bar{\mathbf{R}} \quad (24)$$

where  $S_{i+1/2}$  is the common surface between volume  $(i, j)$  and volume  $(i + 1, j)$ . Defining the flux of tensor  $\boldsymbol{\Pi}$  over the control surface  $\mathcal{F}(\bar{\mathbf{U}})$  as

$$\mathcal{F}(\bar{\mathbf{U}})_{i,j} = (\boldsymbol{\Pi} \cdot \mathbf{S})_{i+1/2} + (\boldsymbol{\Pi} \cdot \mathbf{S})_{i-1/2} + (\boldsymbol{\Pi} \cdot \mathbf{S})_{j+1/2} + (\boldsymbol{\Pi} \cdot \mathbf{S})_{j-1/2} \quad (25)$$

where  $\mathbf{S}$  is the surface vector, the spatial approximation of Eq. (24) is

$$\Delta \bar{\mathbf{U}}_{i,j} = -\frac{\Delta t}{V_{i,j}} \left[ \mathcal{F}(\bar{\mathbf{U}})_{i,j} - \mathcal{D}(\bar{\mathbf{U}})_{i,j} \right] + \Delta t \bar{\mathbf{R}} \quad (26)$$

where  $\mathcal{D}(\bar{\mathbf{U}})_{i,j}$  is an artificial dissipation. It is important to note that Eq. (26) is a spatial approximation of Eq. (24) because tensor  $\boldsymbol{\Pi}$  is considered constant over each of the four control surfaces that define the control volume.

In order to calculate  $\mathcal{F}(\bar{\mathbf{U}})_{i,j}$ , the flux of tensor  $\boldsymbol{\Pi}$  through the control surfaces must be calculated. The explicit form of this calculation as well as the implementation of the artificial dissipation,  $\mathcal{D}(\bar{\mathbf{U}})_{i,j}$ , is given by Bobenrieth Miserda and Mendonça (2005). For the time marching of Eq. (26), a third-order Runge-Kutta is used as proposed by Shu, Yee (1997). This yield to

$$\bar{\mathbf{U}}^1 = \bar{\mathbf{U}}^n - \frac{\Delta t}{V_{i,j}} \left[ \mathcal{F}(\bar{\mathbf{U}}^n) - \mathcal{D}(\bar{\mathbf{U}}^n) \right] + \Delta t \bar{\mathbf{R}}^n \quad (27)$$

$$\bar{\mathbf{U}}^2 = \frac{3}{4} \bar{\mathbf{U}}^n + \frac{1}{4} \bar{\mathbf{U}}^1 - \frac{1}{4} \left\{ \frac{\Delta t}{V_{i,j}} \left[ \mathcal{F}(\bar{\mathbf{U}}^1) - \mathcal{D}(\bar{\mathbf{U}}^1) \right] + \Delta t \bar{\mathbf{R}}^1 \right\} \quad (28)$$

$$\bar{\mathbf{U}}^{n+1} = \frac{1}{3} \bar{\mathbf{U}}^n + \frac{2}{3} \bar{\mathbf{U}}^2 - \frac{2}{3} \left\{ \frac{\Delta t}{V_{i,j}} \left[ \mathcal{F}(\bar{\mathbf{U}}^2) - \mathcal{D}(\bar{\mathbf{U}}^2) \right] + \Delta t \bar{\mathbf{R}}^2 \right\} \quad (29)$$

As used in this work, the resulting numerical method is fourth-order accurate in space and third-order accurate in time.

#### 4. Results

In order to analyze the effects of the oscillating motion, is realized a study of several cases and for each one of these the Mach number is set to 0.2 and the Reynolds number to 100. For the definition of each one of the cases is generated a combination of two created key parameters, the vertical velocity of reference and the angular frequency of reference, respectively defined as

$$V_{ref} = \frac{v_{max}}{U_{\infty}} \quad , \quad \omega_{ref} = \frac{\omega_y}{\omega_s} = \frac{\omega_y}{2\pi St} \quad (30)$$

where  $\omega_s$  is the angular frequency related to the simulated vortex-emission frequency of the static circular cylinder at the same Mach and Reynolds numbers, represented by the Strouhal number,  $St$ , in Eq. (30). From previous research, the value of this Strouhal number is known to be 0.15. Being so, when the angular frequency of reference is set to one, it results in an oscillating motion with a frequency equal to the vortex-emission frequency of the static case.

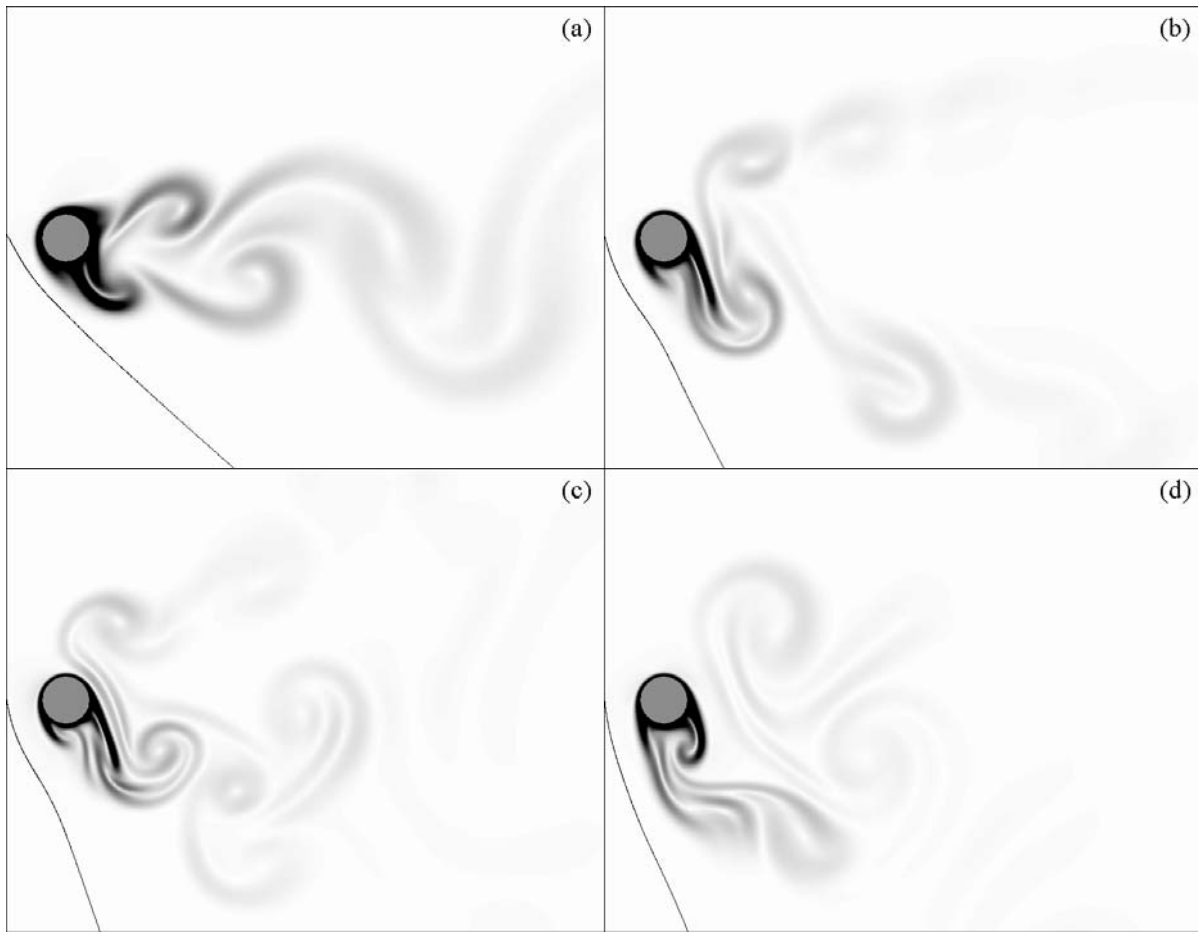


Figure 1. Visualizations of the oscillation motion for four different cases: (a) -  $V_{ref}$  set to 1.0 and  $\omega_{ref}$  set to 2.0, (b) -  $V_{ref}$  and  $\omega_{ref}$  set to 2.0, (c) -  $V_{ref}$  and  $\omega_{ref}$  set to 3.0, (d) -  $V_{ref}$  set to 3.0 and  $\omega_{ref}$  set to 1.0.

Figure (1) shows visualizations of the oscillation motion for four different cases, Fig. (1a) to (1d), at the maximum upward velocity instant, the inserted streamline helps at this determination. The plotted variable is the nondimensional magnitude of the temperature gradient. In the visualizations, white corresponds to 0 and black corresponds to 0.6. Each one of the above visualizations corresponds to one of the four distinct kind of cases studied. Figure (1a) displays a very regular and defined Von-Kármán vortex street, showing a periodic and symmetric vortex system topology. In a similar way, Fig. (1b) shows a well defined vortex street that looks like the Von-Kármán one, but in this case there is an oblique asymmetry between the vortices emitted in the upper and lower position of the cylinder that reveals a periodic although anti-symmetric vortex system topology. Different from the first two visualizations, Fig. (1c) and (1d) no longer show a well defined vortex street. However, in the visualization displayed in Fig. (1c) is still possible to see some periodicity of the vortex-street, revealing a pre-chaotic state of the system. In Fig. (1d) no periodicity is noticeable and a much disorganized vortex-street is present, characterizing a chaotic state of the vortex street topology.

These characteristics can also be appreciated in Fig. (2) that shows the unsteady lift force coefficient as a function of time. In Fig. (2) the black signal corresponds to instantaneous values and the gray corresponds to mean values of the lift coefficient. Figure (2a) and (2b) shows a very periodic behavior of the instantaneous signal that is directly associated with the well defined vortex street of these two particular cases. However, different from Fig. (2a), Figure (2b) no longer shows a mean signal floating around zero. This unique characteristic shows that the oblique asymmetry of the vortex street, Fig. (1b), generates a non-null resulting lift coefficient over the cylinder's surface. The instantaneous signal of Fig. (2c) shows a non-linear response of the lift coefficient, but still has a slightly periodic behavior, showing the transition from a periodic to chaotic state of the system. In Fig. (2d) is displayed the chaotic response of the lift coefficient that is associated with a very disorderly vortex-street.

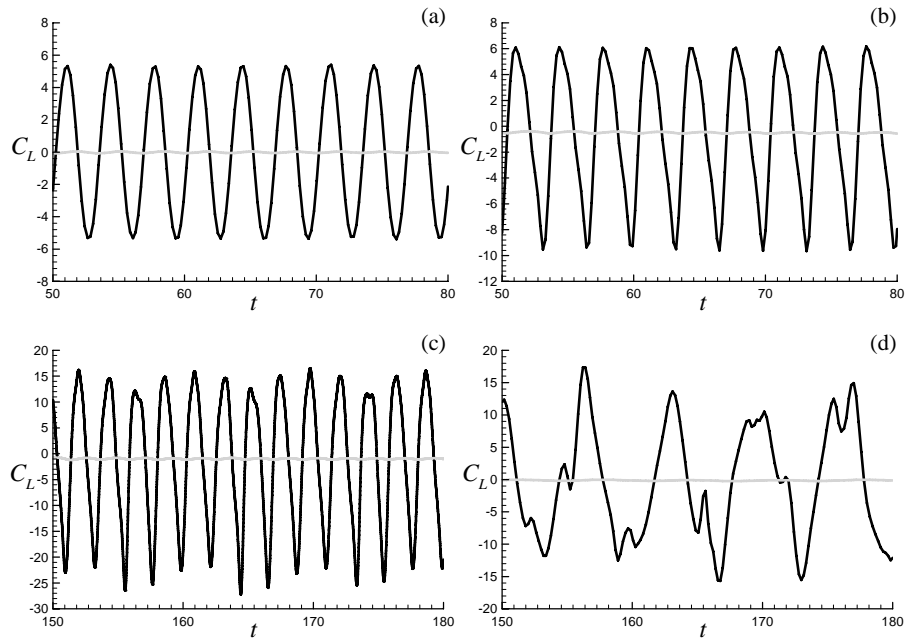


Figure 2. Unsteady lift force coefficient as a function of time: (a) -  $V_{ref}$  set to 1.0 and  $\omega_{ref}$  set to 2.0, (b) -  $V_{ref}$  and  $\omega_{ref}$  set to 2.0, (c) -  $V_{ref}$  and  $\omega_{ref}$  set to 3.0, (d) -  $V_{ref}$  set to 3.0 and  $\omega_{ref}$  set to 1.0.

Figure (3) shows the phase diagram for the unsteady lift coefficient. The phase path in the diagram of Fig. (3a) and in the one of Fig (3b) are very well defined as a consequence of a very well behavior of the system. In Fig. (3b) is also noticeable the presence of a non-null lift coefficient as the phase diagram is not centered at 0, in the horizontal axis. In Fig. (3c) is observed a intense deviation of the phase paths occasioned by the temporal variation of the maximum and minimum values of the lift coefficient, but is not entirely disorganized, emphasizing the transition from a periodic state to a chaotic one. Figure (3d) shows a phase diagram, in which the phase path follows no pattern and reveals the completely disorderly state of the system.

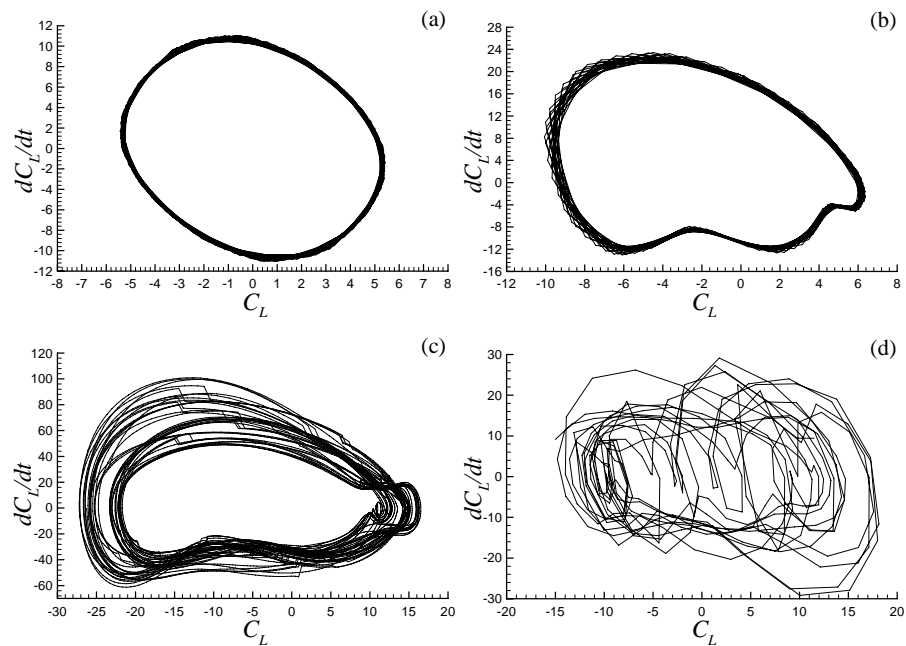


Figure 3. Phase diagram for the unsteady lift coefficient: (a) -  $V_{ref}$  set to 1.0 and  $\omega_{ref}$  set to 2.0, (b) -  $V_{ref}$  and  $\omega_{ref}$  set to 2.0, (c) -  $V_{ref}$  and  $\omega_{ref}$  set to 3.0, (d) -  $V_{ref}$  set to 3.0 and  $\omega_{ref}$  set to 1.0

The power spectrums for the unsteady lift coefficient of the four cases focused in the present work are showed in Fig. (4). The power spectrum of the first two cases, Fig. (4a) and (4b), shows only the fundamental frequency associated with low energy sub-harmonics. On the other hand, for the last two, Fig. (4c) and (4d), the spectrum is broader close to the fundamental frequency, becoming impossible to make a precise definition of sub-harmonics. This particular characteristic is caused by the non-linearity of the system in the two cases corresponding to Fig. (4c) and (4d).

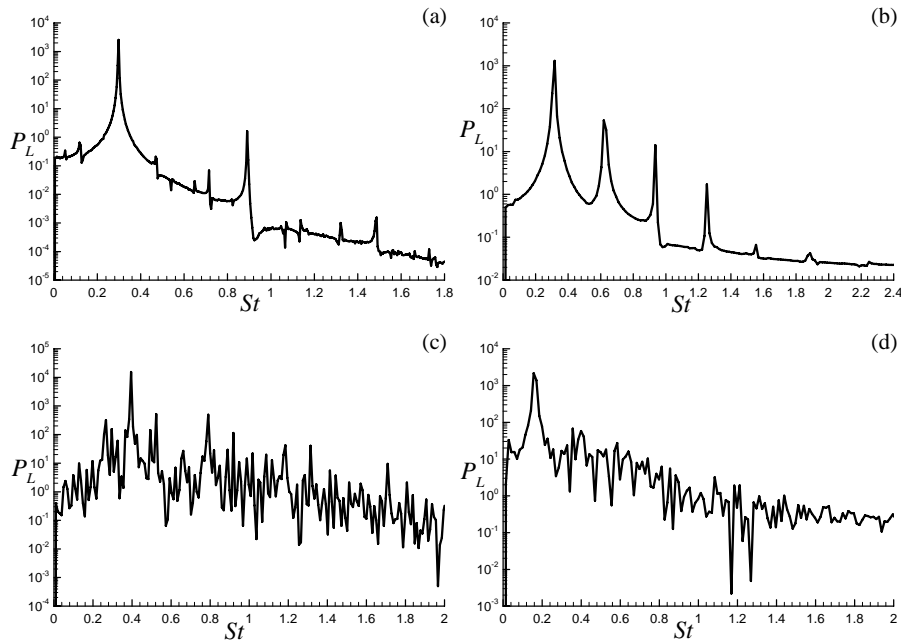


Figure 4. Power spectrum for the unsteady lift coefficient: (a) -  $V_{ref}$  set to 1.0 and  $\omega_{ref}$  set to 2.0, (b) -  $V_{ref}$  and  $\omega_{ref}$  set to 2.0, (c) -  $V_{ref}$  and  $\omega_{ref}$  set to 3.0, (d) -  $V_{ref}$  set to 3.0 and  $\omega_{ref}$  set to 1.0

Figure (5) shows a classification of all the studied cases, based on each one's vortex system topology (symmetric and anti-symmetric) and phase behavior of the unsteady lift coefficient (periodic, pre-chaotic and chaotic). These criteria results in four groups, namely the periodic and symmetric, periodic and anti-symmetric, pre-chaotic and chaotic cases. In this figure four linking lines are also shown. The first (horizontal) line links the cases where  $V_{ref} = 1.0$ . The second (vertical) line links the cases where  $\omega_{ref} = 1.0$ , and the third (oblique, with a 45° inclination) line, links the cases where the amplitude of motion is held constant. The fourth (oblique, with a 135° inclination) line links the cases that are orthogonal to the previous line. These cases were studied in order to define the local limit of the periodic and anti-symmetric behavior.

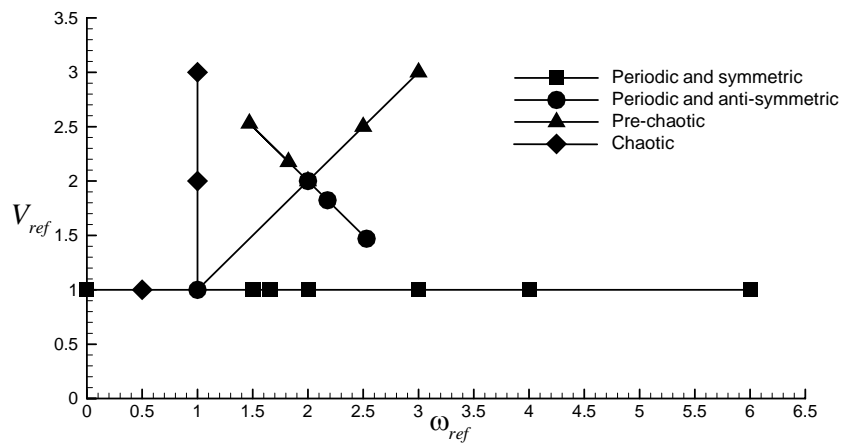


Figure 5. Classification of the cases studied, based on the topology of the vortex wake (symmetric and anti-symmetric) and the phase behavior of the unsteady lift coefficient (periodic, pre-chaotic and chaotic).

As we advance from the first case ( $\omega_{ref} = 0.0$ ) to the last one over the first (horizontal) line ( $\omega_{ref} = 6.0$ ), the system becomes more periodic and symmetric, except the case  $\omega_{ref} = 1.0$ , where the system shows itself to be periodic and anti-symmetric, and the case  $\omega_{ref} = 0.5$ , where the system has a chaotic behavior. This growing periodicity of the system is due to the fact that the system approaches a quasi-static situation, as the oscillation frequencies become higher than the static vortex-emission frequency. These high frequencies are also associated to very small amplitudes of motion.

Figure (5) also shows the higher sensibility to changes into the maximum linear velocity of oscillation when compared to changes into the angular frequency of oscillation. This higher sensibility is due to the fact that a small increment of 1.0 in  $V_{ref}$ , when  $\omega_{ref}$  remains constant, results in the completely disorganization of the system, the system moves from a periodic state to a chaotic one. In contrast, an increment of 6.0 in  $\omega_{ref}$ , when  $V_{ref}$  remains constant, not only keeps the system stable and periodic, but also makes the system even more stable as it moves forward a quasi-static situation.

## 5. Conclusions

In the present work is proposed a methodology, used to simulate the laminar flow over a normally oscillating circular cylinder, created by the insertion of pseudo-force and pseudo-work terms to the momentum and energy equations, respectively, to solve the system of governing equations from a non-inertial frame of reference fixed at the cylinder., as proposed by Bobenrieth Miserda e Mendonça (2005). In order to analyze the effects of the oscillating motion, two key parameters,  $V_{ref}$  and  $\omega_{ref}$ , were created, and different combination of these two parameters resulted into four groups of cases: Periodic and symmetric, Periodic and anti-symmetric, Pre-chaotic and Chaotic.

The cases with a periodic and symmetric behavior, concentrated over the line in which  $\omega_{ref}$  is constant and equal to 1.0, showed a very well define vortex-street associated with a signal of the unsteady lift coefficient that has a periodic and quasi-linear behavior resulting in a phase diagram with a well define phase path and a power spectrum, that shows, with definition, the fundamental frequency of the related case and sub-harmonics of low energy. Similar to these cases, the ones with a Periodic and anti-symmetric behavior, also showed a well defined vortex-street associated with a periodic and quasi-linear signal of the unsteady lift coefficient. However, the vortex-street topology revealed an oblique asymmetry that resulted into a non-null lift coefficient over the cylinder's surface.

On the other hand, the cases with a pre-chaotic behavior, although showed a slightly periodicity, were in a transition state between periodic and chaotic, showing a complex vortex-street, as theirs phase diagram displayed phase paths with great deviation, but they still seemed to follow a certain pattern, and their power spectrum no longer showed, with clear definition, the fundamental frequency and sub-harmonics. The chaotic cases no longer showed any periodic behavior of the unsteady lift coefficient signal associated with a complex and disorderly vortex street that resulted in a phase diagram without any pattern and a power spectrum that also makes impossible to clearly define the fundamental frequency and sub-harmonics.

The system also showed a higher sensibility to changes into the maximum linear velocity of oscillation when compared to changes into the angular frequency of oscillation. This emphasizes the importance of the maximum velocity of oscillation and the maximum amplitude of oscillation as they showed to be critical parameters. Any small increment of these parameters, at a fixed frequency of oscillation, can bring serious structure damage as they rapidly remove the system stability.

## 6. References

- Anderson, D. A., Tannehill, J. C. and Pletcher, R. H., Computational Fluid Mechanics and Heat Transfer, 1st ed., Hemisphere Publishing Corporation, New York, 1983, Chap. 5.
- Batchelor, C. K., 1983, An Introduction to Fluid Dynamics, 1st ed., University Press, Cambridge, 1983, Chap. 3.
- Blackburn H. M., Henderson R.D., "A Study of Two-Dimensional Flow Past an Oscillating Cylinder", 1999, Journal of Fluid Mechanics, Vol. 385, pp. 255 - 286.
- Bobenrieth Miserda, R.F., Mendonça, A.F. de, "Numerical Simulation of the Vortex-Shock Interactions in a Near-Base Laminar Flow", AIAA 43rd Aerospace Sciences Meeting and Exhibit, AIAA 2005-0316, Reno, Nevada, 2005.
- Jared S. C. et al, "Computation of Vortex Shedding and Radiated Sound for a Circular Cylinder", 4th International Symposium of Fluid-Structure Interactions, Aeroelasticity, Flow-Induced Vibration and Noise, Dallas, Texas, November 16 - 21, 1997.
- Yee, H. C., "Explicit and Implicit Multidimensional Compact High-Resolution Shock-Capturing Methods: Formulation," Journal of Computational Physics, Vol. 131, No. 1, 1997, pp. 216, 232.